JOURNAL OF GEOPHYSICAL RESEARCH, VOL. 89, NO. B7, PAGES 5987–6002, JULY 10, 1984

Geoid Anomalies in a Dynamic Earth

MARK A. RICHARDS AND BRADFORD H. HAGER

Seismological Laboratory, California Institute of Technology, Pasadena

In order to obtain a dynamically consistent relationship between the geoid and the earth's response to internal buoyancy forces, we have calculated potential and surface deformation Love numbers for internal loading. These quantities depend on the depth and harmonic degree of loading. They can be integrated as Green functions to obtain the dynamic response due to an arbitrary distribution of internal density contrasts. Spherically symmetric, self-gravitating flow models are constructed for a variety of radial Newtonian viscosity variations and flow configurations including both whole mantle and layered convection. We demonstrate that boundary deformation due to internal loading reaches its equilibrium value on the same time scale as postglacial rebound, much less than the time scale for significant change in the convective flow pattern, by calculating relaxation times for a series of spherically symmetric viscous earth models. For uniform mantle viscosity the geoid signature due to boundary deformations is larger than that due to internal loads, resulting in net negative geoid anomalies for positive density contrasts. Geoid anomalies from intermediate-wavelength density contrasts are amplified by up to an order of magnitude. Geoid anomalies are primarily the result of density contrasts in the interior of convecting layers; density contrasts near layer boundaries are almost completely compensated. Layered mantle convection results in smaller geoid anomalies than mantle-wide flow for a given density contrast. Viscosity stratification leads to more complicated spectral signatures. Because of the sensitivity of the dynamic response functions to model parameters, forward models for the geoid can be used to combine several sources of geophysical data (e.g., subducted slab locations, seismic velocity anomalies, surface topography) to constrain better the structure and viscosity of the mantle.

INTRODUCTION

The relationship between large-scale geoid anomalies and thermally driven flow in the earth's mantle was discussed almost 50 years ago by *Pekeris* [1935]. He showed that the gravitational effect of the surface deformation caused by the flow is opposite in sign and comparable in magnitude to that of the driving density contrast. Consequently, in a viscous earth the net gravity or geoid anomaly is also dependent in both sign and magnitude upon the dynamics of the mantle. This represents a complete departure from the result for a rigid or elastic earth in which positive internal density contrasts are always associated with positive gravitational anomalies.

Studies of postglacial rebound [e.g., *Haskell*, 1935; *Cathles*, 1975] as well as the very existence of plate motions show that the mantle responds to stresses applied over geologic time scales by slow creeping flow. Therefore any interpretation of long-wavelength geoid anomalies should include the dynamical effects first described by *Pekeris* [1935]. These effects, particularly boundary deformation caused by flow, have been investigated by *Morgan* [1965], *McKenzie* [1977], and *Parsons and Daly* [1983] for intermediate-wavelength features using two-dimensional models with uniform mantle viscosity. *Runcorn* [1964, 1967] addressed the relationship between long-wavelength gravity anomalies and the flow field in a self-gravitating, uniform viscous sphere. Each of these studies showed that the deformation of boundaries, especially the upper surface, has a major effect upon the net gravity or geoid anomaly arising from a density contrast at depth. Moreover, the effects of viscosity stratification and layered convection in the mantle can significantly alter the calculated relationship between geoid elevations and driving density contrasts [*Richards and Hager*, 1981; *Ricard et al.*, 1983].

In this paper, we develop and discuss several dynamical models and their implications for geoid interpretation. The aim is to provide quantitative relationships between density contrasts within the earth and other geophysical observables, including boundary topography, as well as the geoid. At the present time we cannot solve the full problem of thermal convection for a given model to determine these dynamical relationships for the whole system (see *McKenzie* [1977] for two-dimensional numerical examples). Since both the temperature structure of the mantle and the temperature dependence of the density and viscosity of mantle minerals are unknown, and since even the geometry of the convective circulation is not known (i.e., whole mantle versus layered convection), a simpler and more direct approach is desirable. If the thermal density anomaly is treated simply as a "load," the resulting surface deformation and geoid anomaly can be determined by solving only the equilibrium equations for a viscous earth.

The standard characterization of the earth's response to tidal loading in terms of Love numbers [*Love*, 1911; *Munk and MacDonald*, 1960] suggests a useful way to characterize dynamic response functions. Love numbers for internal loading of the earth are obtained by normalizing residual geoid anomalies and boundary deformations by the gravitational potential of the driving load. We obtain these quantities as functions of the depth and harmonic degree of the load, thus yielding Love numbers that are equivalent to Green functions.

A major question currently is whether chemical stratification of the mantle, associated with the 670-km seismic discontinuity, presents a barrier to vertical flow and divides the mantle into separately convecting layers. In order to address this issue our flow models include not only radial viscosity variations but also the possibility of either mantle-wide or chemically stratified flow in the mantle as illustrated in Figure 1. Both the geoid and boundary deformation response functions (Love numbers) show a strong model dependence. For example, for mantle-wide flow, positive driving density contrasts cause net negative geoid anomalies for uniform mantle viscosity, since the negative anomaly caused by upper surface deformation overwhelms the geoid anomaly due to the density

Paper number 4B0594.
0148-0227/84/004B-0594$05.00

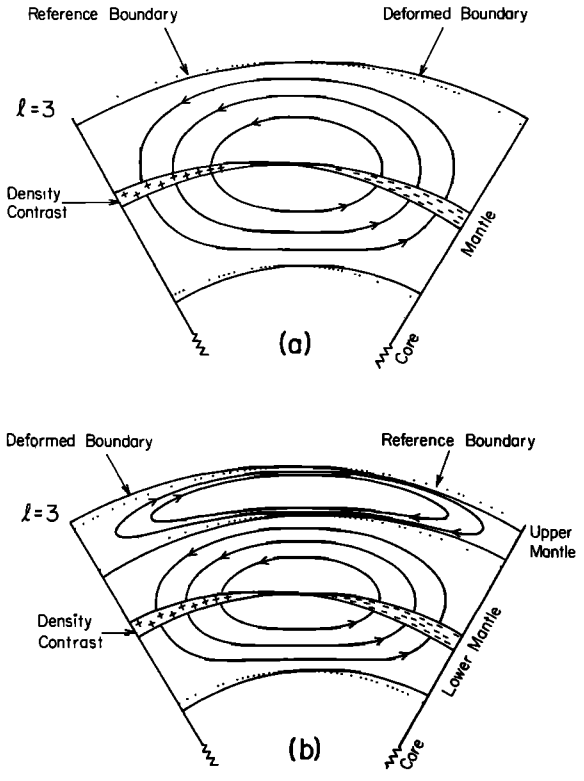

Fig. 1. Illustrations of flow models for spherical earth calculations ($l = 3$). (*a*) Whole mantle flow. (*b*) Flow with a chemical barrier at the 670-km discontinuity. Plus and minus signs indicate positive and negative density contrasts. The dashed lines are reference boundaries, and the solid lines represent the displaced boundaries. Streamlines indicate the sense of flow.

contrast itself. However, net positive geoid anomalies are obtained for a channel of sufficiently low viscosity in the upper mantle. This occurs because low upper mantle viscosity reduces the deformation of the upper surface. The core-mantle boundary deformation increases but has less effect upon the geoid because of its great depth. As shown in Figure 1*b*, the layered flow case introduces much more complicated behavior. It is precisely this strong model dependence that makes these models useful in geodynamics. The observed spectral and loading-depth dependence of these response functions can be used to discriminate among various proposed models for mantle structure and rheology.

Although observations of satellite orbits provided the means for determining the lower-order harmonics of the geopotential over two decades ago [*Kaula*, 1963*a*; *Guier*, 1963], subsequent efforts to interpret the long-wavelength geoid have been largely unsuccessful. Some correlations with tectonic features have been suggested [e.g., *Kaula*, 1972], notably a general correspondence between subduction zones and geoid highs. *Chase* [1979] and *Crough and Jurdy* [1980] demonstrated a remarkable correlation between the spatial distribution of hot spots and the nonhydrostatic second harmonic geoid. *Hager* [this issue] has shown that the fourth through ninth geoid harmonics are strongly correlated with the seismicity-inferred presence of subducting slabs, thus yielding quantitative estimates over a definite spectral range for the dynamic response functions which are the subject of this paper. Additionally, recent seismological determinations of lateral variations in seismic velocities [e.g., *Nakanishi and Anderson*, 1982; *Dziewonski*, this issue; *Clayton and Comer*, 1983] provide another powerful constraint on geoid interpretation, and a large amount of information on crustal thickness, topography, and density have yet to be considered in relation to the geoid. It is therefore resonable to expect increasingly accurate and useful observations of the earth's density anomalies and effective boundary deformations. Cast in the form of dynamic response functions as discussed in this paper, these data provide means for discriminating among various dynamic models for the mantle.

MODELING CONSIDERATIONS

Quantitative models for the geoid derive from constitutive laws, equations of motion and material continuity, and boundary conditions. It is impossible at the present time to specify fully the earth's rheology or to solve all these equations exactly. We must make various approximations and assumptions in developing mathematical models; in doing so we try to include the important physical effects while avoiding unnecessary complication in the method of solution. In this section we discuss our assumptions concerning mantle rheology and flow, boundary conditions, and the thermal driving forces involved. Boundary deformation is afforded a detailed treatment in a separate section.

Rheology and Flow

The selection of appropriate models for the mechanical behavior of the lithosphere, mantle, and core depends upon both the time and length scales involved. Here we are interested in length scales for which lithospheric strength is negligible, roughly defining what is meant by "long-wavelength" geoid anomalies, and time scales of the order of those required for substantial changes in the convective flow pattern in the mantle. As we show below, this implies harmonic degrees l less than 40 (wavelengths greater than 1000 km). If mantle flow is reflected in plate motions, the mantle flow pattern is stable for times far in excess of 1 m.y., which we take as a characteristic time scale. The core is inviscid for the time scales of interest here; it may also be assumed to be in a state of hydrostatic equilibrium.

The lithosphere presents several problems, including those of finite elastic strength and of lateral variations in rheological properties, density, and thickness. For loads of wavelength greater than about 1000 km the elastic strength of the lithosphere is negligible [*McKenzie and Bowin*, 1976; *Watts*, 1978] so that surface loads are supported by buoyancy and the resulting flow in the mantle. The lithosphere is essentially transparent to long-wavelength normal tractions from flow in the mantle.

Lateral variations in rheological properties of the lithosphere are responsible for the plate tectonic style of convection in the earth's mantle. The plates move as distinct units with respect to each other and effectively form a rigid lid for any sublithospheric small-scale convection which may exist. Plate boundaries, on the other hand, are relatively weak, allowing the plates themselves to participate in mantle convection [*Hager and O'Connell*, 1981]. This lateral heterogeneity of the effective viscosity of the lithosphere allows density contrasts in the interior to excite significant toroidal flow [*Hager and O'Connell*, 1978] not just the poloidal flow which would result from a mantle with spherically symmetric viscosity structure.

The choice of boundary conditions at the surface is not obvious, and the analytical technique we use here does not account for lateral viscosity variations. We argue that the mechanical effect of the lithosphere on small-scale flow beneath

plate interiors can be represented by a no-slip boundary condition at the earth's surface. Flow involving the plates themselves is probably best approximated by a free-slip boundary condition. We present calculations for both cases and find that the results are similar. This suggests that a more complicated boundary condition that would better represent the effects of lithospheric plates would also be similar.

The effect on the geoid of lateral variations in lithospheric thickness and density has been discussed by *Chase and McNutt* [1982] and *Hager* [1983]. These variations are primarily the result of variations in crustal thickness and in the age of the lithosphere. Since they are close to the surface, they are generally well compensated, and their effect on the geoid is small (less than 20 m out of a total geoid variation of greater than 200 m). However, their effect on topography is large. If surface deformation and the geoid are to be used concurrently to obtain sublithospheric density contrasts as discussed below, corrections must be made to compensate for the topographic effects of large density contrasts within the lithosphere.

The appropriate constitutive law (or laws) for modeling flow in the mantle cannot be determined with certainty at the present time. Possible creep mechanisms for deformation of mantle minerals include dislocation climb [*Weertman*, 1968], which implies a nonlinear rheology, and grain boundary diffusion or superplasticity [*Twiss*, 1976; *Ashby and Verrall*, 1977; *Berckhemer et al.*, 1979], which at low stress levels might result in a linear relationship between shear stress and strain rate. Mathematical tractability has led most researchers to employ linear rheology, either Maxwellian or Newtonian, in modeling flow in the mantle. Furthermore, for some surface loading problems in which the magnitude of shear stress decays with depth, nonlinear rheology might not be distinguishable from layered linear rheology; the lower stress levels found at depth would correspond to higher apparent viscosity. Estimates for effective mantle viscosity have been obtained for a variety of loading problems. Values given for average mantle viscosity have generally been of the order of 10^{21} Pa s (10^{22} P) [*O'Connell*, 1971; *Cathles*, 1975; *Peltier*, 1976; *Yuen et al.*, 1982], although estimates as small as 10^{18} Pa s have been obtained for the upper mantle or asthenosphere for loads of smaller scale [*Passey*, 1981]. Although viscoelastic models have found application to shorter-term problems such as glacial loading and unloading [*Clark et al.*, 1978; *Wu and Peltier*, 1982], the time scales of 1 m.y. or greater of interest here are in excess of Maxwell times for the mantle so we ignore elastic effects. For the purpose of exploring the basic physics of internal loading problems and for mathematical simplicity, we employ Newtonian models in which viscosity is dependent upon depth only, although when this theory is applied to actual data, the results suggest that lateral variations in effective viscosity may be important.

Boundary Conditions

Three possible boundaries are considered in our spherically symmetric, layered earth models: (1) the core-mantle boundary, (2) the upper surface, and (3) a change in composition and/or viscosity across the 670-km seismic discontinuity.

We model the core-mantle boundary as one at which there is no shear traction and no steady state vertical transport. As discussed above, the mantle-lithosphere boundary is more complicated. We have investigated both no-slip and free-slip conditions and have included both types in the results presented here, although, as we noted above, the difference between the two is not profound.

Chemical stratification and multilayer convection have been suggested [e.g., *Anderson*, 1979] to explain the major seismic discontinuity at 670 km. Geochemical budget models as well as the lack of seismicity below 670 km are thought by some to suggest that upper mantle flow does not penetrate this level [*Jacobsen and Wasserburg*, 1980; *Richter and McKenzie*, 1981]. We include the effect of such a boundary in our investigation in order to understand how geoid and geodetic data might be used to test the chemical layer hypothesis. A chemical discontinuity is modeled by setting the (steady state) vertical velocity to zero at the boundary; horizontal velocities and normal and shear tractions are continuous. This results in a two-layer, shear-coupled, antisymmetric flow system, as illustrated in Figure 1*b*. Another possibility associated with both the 400- and 670-km discontinuities is that of an abrupt phase change within the mantle, which in the simplest case might be modeled as a spike in the compressibility curve for the mantle assuming that the transition is adiabatic and ignoring thermal effects. We have not treated this case since compressibility introduces nonlinearity into the field equations and makes solutions much more difficult to obtain.

Driving Forces and Loads

The relationships among loading, gravity, and deformation can be obtained without solving for the thermodynamics. This is accomplished by calculating the flow driven by arbitrary density contrasts at any given depth. Kernels (Love numbers) representing the viscous response functions so obtained can then be integrated over depth in accordance with any prescribed distribution of thermal density anomalies; the linearity of the problem (with the caveat of linear, spherically symmetric viscosity) allows for superposition of solutions. Our method is to solve for loading due to a surface density contrast at a given depth and spherical harmonic degree, thereby characterizing the response as a function of spatial wavelength and depth in the mantle. In this way we can isolate the relationships desired for geophysical observables from the thermal part of the convection problem.

The Field Equations

With the above qualifications and simplifications we can specify tractable field equations to investigate the loading problem for a variety of rheological and structural configurations in the mantle. The mantle will be assumed to behave as a self-gravitating, spherically symmetric, incompressible, Newtonian viscous fluid. Since the Reynold's number is very large owing to the mantle's high viscosity, inertial or time-dependent terms are omitted from the equations of motion. The only time dependence is introduced by changes in position with time of the driving density contrasts and relaxation of the boundaries to a steady state condition of deformation. We address the relaxation problem in detail in Appendix 2, the result being that boundary deformations decay rapidly compared to the time scale of flow in the interior.

The equations of motion can be written

$$\nabla \cdot \boldsymbol{\tau} + \rho \mathbf{g} = 0 \tag{1}$$

where $\boldsymbol{\tau}$ is the stress tensor, ρ the density, and $\mathbf{g}$ the gravitational acceleration. The mantle will be assumed to be incompressible throughout; although radial density layering can be arbitrarily imposed in our method of solution, allowance for finite fluid compressibility is mathematically difficult and is generally ignored by most authors [*Cathles*, 1975; *Peltier*,

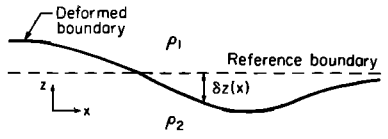

Fig. 2. Illustration of the geometry for the analytical treatment of deformation of the boundary between two fluid half spaces with densities ρ_1 and ρ_2. The actual boundary (solid line) is displaced an amount $\delta z(x)$ from the reference boundary (dashed line).

1981] since the dynamic effect is probably small [*Jarvis and McKenzie*, 1980]. *Ricard et al.* [1983] have shown that the effect of compression from lateral gravity variations is negligible. The incompressible continuity equation is

$$\nabla \cdot \mathbf{v} = 0 \tag{2}$$

where $\mathbf{v}$ is the velocity vector. The Newtonian constitutive relation is

$$\tau = -p\mathbf{I} + 2\eta\varepsilon \tag{3}$$

where p is the pressure, $\mathbf{I}$ the identity matrix, η the viscosity, and ε the strain rate tensor.

For global scale-loading problems, self-gravitation effects cannot be ignored [*Love*, 1911; *Clark et al.*, 1978]. The gravitational effects of deformed boundaries must be included in any self-consistent model. The gravitational potential V must satisfy

$$\nabla^2 V = 4\pi G\rho \tag{4}$$

where we have chosen the sign convention such that $g = -\nabla V$. These equations are linear in all the variables and can be straightforwardly solved by either propagator matrix [*Hager and O'Connell*, 1981] or numerical techniques. Before proceeding to a fully three-dimensional (spherical) solution, we present some useful results from the simple two-dimensional half-space problem. Results from the viscous relaxation problem that justify the hypothesis of steady state flow are given in Appendix 2.

Analytical Treatment of Boundary Deformation

Loading of the earth by gravitational potential (e.g., tidal loading), by external loads (e.g., glacial loading), or internal density contrasts (e.g., thermal convection) will produce deformations of both the surface and any internal boundaries. In this section we analytically treat boundary deformation to first-order accuracy and derive some useful results for the two-dimensional problem. Figure 2 illustrates the warping of a material boundary relative to its deformed or reference state, with densities ρ_1 and ρ_2 above and below the boundary, respectively. The velocity and stress fields must be continuous at the deformed boundary. However, our solution technique requires that we propagate solution vectors from one horizontal boundary to the next, so we require expressions for the velocity and stress fields at the reference (undeformed) boundaries. If the magnitude of deformation, δz, is sufficiently small compared to the thickness of either of the adjacent layers and the spatial wavelength, λ, of interest (as in this study), any variable, u^i in medium i, may be continued, to first-order accuracy, from the deformed boundary to the reference level by

$$u_{\text{ref}}{}^i = u_{\text{def}}{}^i - \frac{\partial u^i}{\partial z}\,\delta z \tag{5}$$

Since flow-induced stresses are always much smaller (first order) than the lithostatic stress level in the mantle (zeroth order), flow and stress variables are first order also; their derivatives behave like the product of first-order terms and the approximate spatial wave number. The only first-order correction due to deformation is the hydrostatic correction to the normal stress:

$$\tau_{zz_{\text{ref}}}{}^i = \tau_{zz_{\text{def}}}{}^i - \rho_i g\,\delta z \tag{6}$$

In passing from the reference boundary as seen in medium 2 to that seen in medium 1, we get an apparent jump in normal stress:

$$\Delta\tau_{zz_{\text{ref}}}{}^{12} = \tau_{zz_{\text{def}}}{}^1 - \tau_{zz_{\text{def}}}{}^2 - \Delta\rho_{12} g\,\delta z \tag{7}$$

where $\Delta\rho_{12} = \rho_1 - \rho_2$. By continuity of stress at the deformed boundary,

$$\Delta\tau_{zz_{\text{ref}}}{}^{12} = -\Delta\rho_{12} g\,\delta z \tag{8}$$

(A similar argument will imply an effective jump in the gravitational acceleration at the reference boundary in the fully self-gravitating spherical case.)

This result can be readily applied to a simple half-space problem. Figure 3 illustrates a surface density contrast (i.e., a thermal density anomaly), $\sigma_d(k)\cos(kx)$, at depth d, exciting flow in a viscous half space of viscosity η and density ρ, with a traction free surface at the top. For simplicity we will first assume that the density contrast is not advected with the resulting flow so that it remains fixed in space (this could be done experimentally using a heat pump, for example). We will then show that the density contrast would not be advected a significant distance in the time it takes for the boundary deformation to reach equilibrium. Solving (1)–(3) using the two-dimensional propagator [*Hager and O'Connell*, 1981], we find that the boundary displacement δz evolves from its initial undeformed position as

$$\delta z = -\frac{\sigma_d(k)\cos(kx)}{\rho}(1 + kd)\exp(-kd)(1 - e^{-t/\tau}) \tag{9}$$

The boundary relaxes with time exponentially toward a steady state of deformation with time constant

$$\tau = 2\eta k/\rho g \tag{10}$$

This is the same time as that derived for the surface loading or unloading problem (e.g., postglacial rebound [*Haskell*, 1935; *Cathles*, 1975]). For example, with $\eta = 10^{21}$ Pa s, $\lambda = 2\pi/k \geq 1000$ km, $\rho = 3.5$ Mg/m^3, $g = 9.8$ m/s^2, we obtain $\tau \leq 11{,}000$ years. Assuming velocities in the mantle of the order of 100 mm/yr or less, we see that mantle transport of at

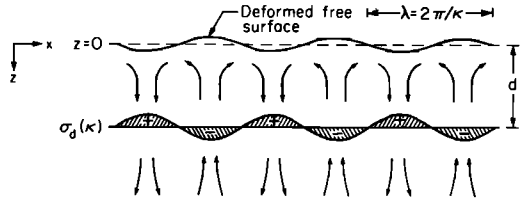

Fig. 3. Illustration of the Fourier flow analysis in a two-dimensional half space. The surface density contrast $\sigma_d(k)\cos(kx)$ at depth d excites flow, resulting in deformation of the free surface. We assume here that the advection of the density contrast by the flow is negligible on the time scale for establishing the boundary deformation.

most a few kilometers (much less than the depth scale of mantle convection) occurs before the free surface is completely relaxed.

Alternatively, we can assume that boundary deformation is rapid and calculate flow velocities under the assumption that vertical flow at the deformed surface vanishes (i.e., boundary deformation is complete). In this case,

$$v_z(d) = -\frac{\sigma_d(k)\cos(kx)}{4\eta} gd \exp(-2kd) \tag{11}$$

Comparing this to the characteristic surface velocity obtained by differentiating (9), we find that

$$\frac{\delta\dot{z}}{v_x(d)} = \frac{2(1+kd)\exp(kd)}{kd} e^{-t/\tau} \tag{12}$$

Once again, we see that long-wavelength boundary deformation is rapid compared to changes in the convective flow pattern independent of $\sigma_d(k)$. Note that this result holds even for "thin" layers which are normally associated with long relaxation times. In Appendix 2 we show that viscous relaxation occurs on a time scale much shorter than that for mantle convection by calculating relaxation times for several spherical earth models.

The long time limit of (9) shows that the effective mass deficit associated with the surface deformation, $\sigma_{\text{eff}} = \rho\delta z$, is of opposite sign and of the same order of magnitude as σ_d. It is now evident for at least two reasons that the assumption that δz is sufficiently small for the application of a linear continuation of the boundary condition is probably justified: (1) Thermal density contrasts in the earth, with the possible exception of subducted slabs, are probably not large enough to cause gross deformation of either internal or external boundaries, and (2) the earth's topography a priori precludes lithospheric deformations greater than 10 km, while seismic data do not suggest large deformations of the core-mantle boundary [*Dziewonski and Haddon*, 1974] or the 670-km discontinuity, although coverage is limited, especially in subduction zones where deformation is expected to be the largest [*Hager*, this issue].

From (9) we can obtain the relationship between the observed gravitational potential and the load as well as the relationship between topography and geoid due to $\sigma_d(k)$. The residual potential calculated at the reference surface contains contributions from both σ_d and σ_{eff}:

$$\delta V^{\text{res}}(z=0) = \delta V^{\text{eff}} + \delta V^{\sigma_d}$$

$$= \frac{2\pi G\cos(kx)}{k}[-(1+kd)+1]\exp(-kd)\sigma_d(k)$$

or

$$\frac{\delta V^{\text{res}}(0)}{\delta V^{\sigma_d}(0)} = -kd \tag{13}$$

This means that for a uniform half space a positive density contrast at depth results in a negative geoid anomaly. The geoid anomaly goes to zero as the density contrast approaches the surface. Furthermore, for depths greater than the wavelength the geoid can be much larger in magnitude than that obtained for a rigid half space for which there would be no boundary deformation. This occurs because the stress that causes boundary deformation falls off less rapidly with the depth of loading than the potential from the load itself.

For spherical models in general the normalized potential

$$K_l(r) = \frac{\delta V_l^{\text{res}}}{\delta V_l^{\sigma}} \tag{14}$$

is the Green function for the earth's surface potential per unit loading at radius r and spherical harmoinic degree l. This quantity is a function of the earth model in general and is related to *Kaula*'s [1963*b*] elastic internal loading potential Love number, k_l'', by

$$K_l(r) = 1 + k_l'' \tag{15}$$

This response function is measurable if the driving density contrasts within the earth are known a priori. *Hager* [this issue] has used this in his discussion of geoid anomalies from subducted slabs, where density contrasts can be estimated. Another application is in comparing seismic velocity heterogeneities to the geoid (B. H. Hager et al., unpublished manuscript, 1984). By assuming a relation between seismic velocity and density the long-wavelength geoid coefficients are obtained from the integral

$$\delta V_l^{\text{geoid}} = \frac{4\pi Ga}{2l+1}\int_{r=0}^{r=a} K_l(r)(r/a)^{l+2}\delta\rho_l(r)\,dr \tag{16}$$

where a is the radius of the earth, $\delta\rho_l(r)$ is the lth harmonic density contrast at radius r, and G is the gravitational constant.

The other observable we can calculate is a dimensionless "impedance," defined as the ratio of geoid elevation to boundary deformation:

$$Z_l(r) = \delta V_l^{\text{geoid}}/g\ \delta r_l \tag{17}$$

where δr_l is the lth harmonic deformation of the surface, and g is the gravitational acceleration. (Note that this is not a true impedance since it involves the observed potential $\delta V_l^{\text{geoid}}$ instead of the driving potential δV^{σ_l}.) Defining a surface deformation Love number h_l'' [e.g., *Munk and MacDonald*, 1960], we have

$$Z_l(r) = 1 + \frac{k_l''}{h_l''}$$

This quantity could be estimated for the surface by taking the ratio of harmonic geoid coefficients to topographic coefficients with the effects of crustal thickness variations removed. To estimate $Z_l(r)$ for a given density distribution and earth model, the numerator and denominator of (17) must be integrated separately.

We have now defined two observables relating the geoid directly to internal loading and earth structure for a density contrast at a given depth. Also, (16) shows how to interpret these quantities for models with distributed density contrasts. We have not yet introduced the gravitational interaction between the load and the mass anomalies due to boundary deformation.

Spherical Earth Models

Formal Solution

Analytical solutions to field equations (1)–(4) with radial variations in viscosity and density and for arbitrary, laterally varying internal loading are given by *Hager and O'Connell* [1981]. Internal density contrasts drive poloidal flow fields for which the relevant stress, flow, and gravitational potential

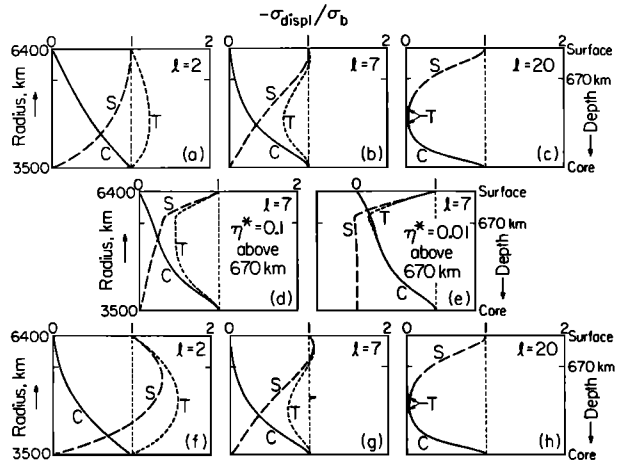

Fig. 4. Mass displacement at the boundaries as a function of loading depth for harmonic degrees 2, 7, and 20 (whole mantle flow). Plots are normalized to a unit density contrast load. The "S" curve is for the upper surface, "C" is for the core-mantle boundary, and "T" is the total mass displaced. Figures 4*d* and 4*e* show the effect of low viscosity in the upper mantle for harmonic degree 7. Figures 4*a*–4*e* are for FF boundary conditions and Figures 4*f*–4*h* are for NF conditions.

variables can be propagated from one radial layer to another according to

$$\mathbf{u}(r) = \mathbf{P}(r, r_0)\mathbf{u}(r_0) + \int_{r_0}^{r} \mathbf{P}(r, \xi)\mathbf{b}(\xi)\, d\xi \tag{18}$$

where $\mathbf{u}$ is the six vector given by

$$\mathbf{u}(r) = \left[v_r,\ v_\theta,\ r\tau_{rr}/\eta_0,\ r\tau_{r\theta}/\eta_0,\ \rho_0 r\delta V/\eta_0,\ \frac{\rho_0 r^2}{\eta_0}\frac{\partial \delta V}{\partial r} \right]^T \tag{19}$$

with radial and tangential velocities v_r and v_θ, normal radial and shear deviatoric stresses τ_{rr} and $\tau_{r\theta}$, perturbed potential δV, and reference density and viscosity ρ_0 and η_0. In these expressions and for the remainder of this paper all dynamical variables contain an implicit spherical harmonic dependence which has been suppressed for simplicity. The 6 × 6 matrix $\mathbf{P}(r, r_0)$ can be expressed analytically [*Gantmacher*, 1960] as a function of r/r_0, normalized layer density $\rho^* = \rho/\rho_0$, normalized layer viscosity $\eta^* = \eta/\eta_0$, and harmonic order l. The driving term for this system is the integral on the right in (18) in which the density contrasts are introduced by

$$\mathbf{b}(r) = [0,\ 0,\ rg(r)\delta\rho(r)/\eta_0,\ 0,\ 0,\ -4\pi r^2 G\rho_0\delta\rho(r)/\eta_0]^T \tag{20}$$

where $g(r)$ is the unperturbed (hydrostatic) gravitational acceleration and $\delta\rho(r)$ is the density contrast at radius r.

The problem is greatly simplified mathematically by casting the driving density structure not only as a sum over spherical harmonics but also as a sum over radial surface density contrasts, that is,

$$\delta\rho(r) = \sum_{b_i} \delta(r - b_i)\sigma_i \tag{21}$$

where $\delta(r)$ is the Dirac delta function and the σ_i are the surface density contrasts. Equation (18) becomes

$$\mathbf{u}(r) = \mathbf{P}(r, r_0)\mathbf{u}(r_0) + \sum_{b_i} \mathbf{P}(r, b_i)\, \mathbf{b}_i \tag{22}$$

where

$$\mathbf{b}_i = [0,\ 0,\ b_i g(b_i)\sigma_i/\eta_0,\ 0,\ 0,\ -4\pi b_i^2 G\rho_0\sigma_i/\eta_0]^T \tag{23}$$

Now, as was indicated previously in (14)–(17), we can characterize all solutions in terms of harmonic order l and radial level or depth of the driving density contrasts since, owing to the linearity of the field equations, these solutions or kernels can be superposed to represent any arbitrary density contrast in the mantle.

A familiar and useful property of the propagator matrix formulation is that solution vectors can be propagated through a series of different material layers by simply forming the product of the individual layer matrices:

$$\mathbf{P}(r, r_0) = \mathbf{P}(r, r_1)\mathbf{P}(r_1, r_{,0}) \tag{24}$$

Therefore changes in viscosity (and density) with depth are easily incorporated into this formalism.

Boundary Conditions

We have discussed two types of boundary conditions: (1) A free-slip (denoted "F") boundary condition requires zero radial velocity (v_r) and zero shear stress ($\tau_{r\theta}$), a condition which applies at the core-mantle boundary, and (2) a no-slip (denoted "N") boundary condition requires zero radial and tangential velocities (v_r and v_θ). Good arguments can be made for applying either of these boundary conditions at the surface. For completeness and to gain insight into the physics of the problem we have modeled both combinations. For example, for no slip at the deformed surface ($r = a + \delta r_a$) and free slip at the core-mantle boundary ($r = c + \delta r_c$), we have, to first order,

$$\mathbf{u}^N(a + \delta r_a) = \left[0,\ 0,\ 0,\ a\tau_{r\theta_a}/\eta_0,\ \rho_0 a\delta V_a/\eta_0,\ \frac{\rho_0 a^2}{\eta_0}\frac{\partial \delta V_a}{\partial r} \right]^T$$

$$\mathbf{u}^F(c + \delta r_c) = \left[0,\ v_{\theta_c},\ c\tau_{rr_c}/\eta_0,\ 0,\ \rho_0 \delta V_c/\eta_0,\ \frac{\rho_0 c^2}{\eta_0}\frac{\partial \delta V_c}{\partial r} \right]^T \tag{25}$$

where we have also set the normal stress to zero at the surface. These boundary conditions apply at the actual deformed boundaries (see Figure 1); however, (22) shows only how to propagate from one spherical reference boundary to another. Therefore (25) must be analytically continued to the reference boundaries via (5)–(8) cast in spherical coordinates. This is a tedious operation which involves finding expressions for τ_{rr_a}, τ_{rr_c}, δV_a, δV_c in terms of the resulting harmonic surface deformations (δr_a, δr_c) and the details as well as the resulting system of equations are included in Appendix 1. This procedure in-

TABLE 1. Model Parameters for Basic Models for Spherical Earth Calculations

Model*	ρ_l	$\delta\rho_{lu}$	ρ_u	η_l, Pas	η_u, Pas	d, km
			Whole Mantle Flow			
A	4.43	0.0	4.43	10^{21}	10^{21}	...
B	4.43	0.0	4.43	10^{21}	10^{19} or 10^{20}	200
C	4.43	0.0	4.43	10^{21}	10^{19} or 10^{20}	670
			Layered Flow			
D	4.92	0.5	3.50	10^{21}	10^{21}	670
E	4.92	0.5	3.50	10^{21}	10^{19} or 10^{20}	670

Parameters include earth and core radii, c and a; core, upper, and lower mantle densities, ρ_c, ρ_u, and ρ_l (in Mg/m^3); upper and lower mantle viscosities, η_u and η_l; effective density jumps at the core-mantle boundary and the 670-km discontinuity, $\delta\rho_{cm}$ and $\delta\rho_{lu}$; and the depth of the upper flow or viscosity layer, d.

*For all models c = 3480 km, a = 6371 km, ρ_c = 11.0, and $\delta\rho_{cm}$ = 4.5.

volves two physical effects: (1) When solution vectors are referenced to the underformed boundaries, there is an apparent jump in normal stress at each boundary given by an expression similar to (8):

$$\delta\tau_{rr} = -\delta\rho g(r)\delta r \tag{26}$$

and (2) there is a similar jump in gravity at each boundary (see Appendix 1). Accordingly, each boundary deformation makes a first-order contribution to the perturbed potential. This occurs because, as demonstrated above, the mass displaced is of the same order of magnitude as the driving density contrast. The important thing to note is that we can cast the problem in a form whose solution gives the deformation of boundaries as well as the gravitational potential at those boundaries as functions of the harmonic order and depth of loading. From these solutions we can generate the desired quantities (Love numbers and impedances) defined by (14)–(17).

Equation (24) shows how to treat layering effects in material properties, but a layered flow system (Figure 1*b*) requires a separate boundary condition at the flow barrier. We model this boundary as a compositional change accompanied by a density jump which results in a simple flow barrier with shear coupling between the two layers. Mathematically, this can be expressed as

$$\mathbf{u}(r + \delta r) = \left[0,\ v_\theta,\ r\tau_{rr}/\eta_0,\ r\tau_{r\theta}/\eta_0,\ \rho_0 T\delta V/\eta_0,\ \frac{\rho_0 r^2}{\eta_0}\frac{\partial \delta V}{\partial r}\right]^T \tag{27}$$

in which the radial velocity is set to zero at the boundary. This also represents another boundary which will deform under loading and an additional apparent jump in normal stress and gravity will occur when (27) is analytically continued to its reference surface (e.g., 670 km depth). For this two-layer flow problem we have two systems of equations (22) that are coupled at an internal boundary whose field variables are given by (27). We have not included the details here, but solution of these propagator equations proceeds straightforwardly, as in Appendix 1, where details are given for the case of whole mantle flow.

RESPONSE FUNCTIONS

The mathematical formalism we have developed for solving the internal loading problem yields solutions in the form of boundary vectors that give the fluid velocities and stresses as well as the gravitational potential and its radial derivative at spherical reference boundaries corresponding to the unperturbed layer boundaries. These reference boundary vectors can be propagated (see equation (18)) to any radial level in the earth, so each solution implicitly contains the stress-flow field and gravitational field throughout the mantle. For any specific model, solutions vary with the depth of loading and harmonic degree so that even for the limited variety of models we have considered here a very large amount of information is generated. The spherical earth results presented in this section are restricted to those involving either the geoid or boundary deformations. The results that follow involve only the approximations discussed above and are analytic, although the resulting algebraic expressions are evaluated on a computer.

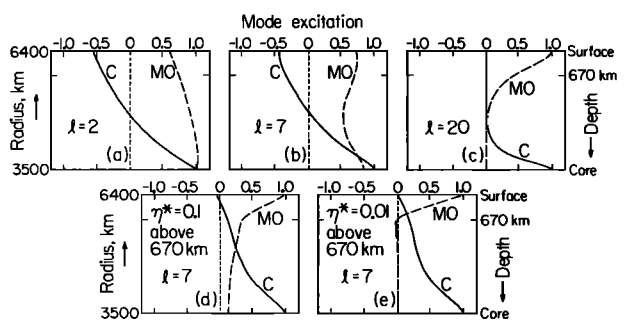

Fig. 5. Viscous normal mode excitation as a function of loading depth for whole mantle models. The "C" (core) and "M0" (mantle) modes are unit normalized, and their excitation amplitudes are plotted for harmonic degrees 2, 7, and 20. Figures 5*d* and 5*e* illustrate the effect of low viscosity in the upper mantle.

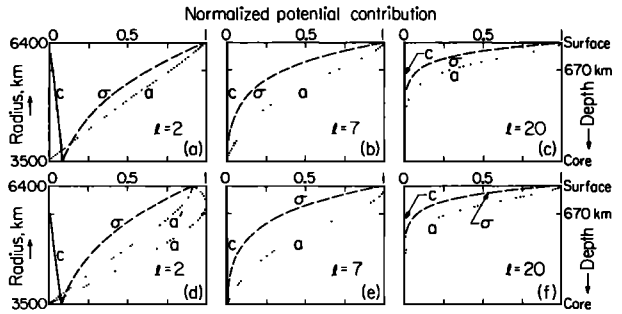

Fig. 6. Relative values of gravitational potential contributions from the density contrast at the indicated depth ("σ"), the deformation of the core-mantle boundary ("c"), and the upper surface deformation ("a") for harmonic degrees 2, 7, and 20. (The "a" and "c" curves actually have opposite sign from the "σ" curve). Values plotted are normalized by the maximum value of curve "a" for convenience in comparison. Figure 6*d* shows the upper surface deformation not corrected for self-gravitation (curve "a'"). Figures 6*a*–6*c* are for FF boundary conditions and Figures 6*d*–6*f* are for NF conditions, all for uniform mantle viscosity.

Whole Mantle Flow

The simplest model is that for mantle-wide flow and most of the physical ideas from spherical modeling can be demonstrated with this model. Figures 4*a*–4*c* show for model A (see Table 1) the amount of mass per unit area, normalized by the amplitude of the load, that is displaced by deformation of the core-mantle boundary and the upper surface as a function of the depth of loading for representative harmonic degrees 2, 7, and 20. The displaced mass is opposite in sign to that of the driving mass anomaly so its negative is plotted for ease in comparison. Figures 4*a*–4*c* are for free-slip at both the core-mantle interface and the upper surface ("FF" case) while Figures 4*f*–4*h* are for no slip at the upper surface ("NF" case). The closer the load is to a boundary the larger are the resulting mass displacement and deformation at that boundary. Also plotted is the total amount of mass displaced at both boundaries. By analogy to the Airy or Pratt principles of isostatic compensation in the lithosphere, these curves represent dynamic isostasy for mantle loads in a spherical earth. The total mass displaced is opposite in sign and comparable, but not identical, in magnitude to that of the load (dashed line) for long wavelengths. For the uniform viscosity model, $-\sigma_{\text{disp}}$ (total)/σ_b is of order unity for $l = 2$ and $l = 7$, but for higher values of l this ratio becomes much smaller if the load is not close to a boundary: this means that the load is almost entirely dynamically supported by flow in the interior. Figures 4*d* and 4*e* show the effects of one and two orders of magnitude

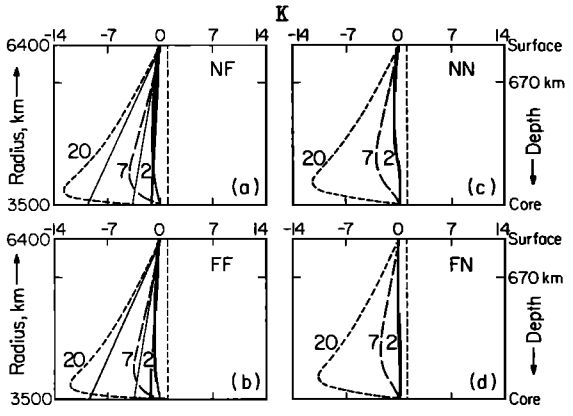

Fig. 7. Surface potential response K as a function of loading depth for harmonic degrees 2, 7, and 20. Illustrated are the four possible combinations of free-slip (F) and no-slip (N) boundary conditions, all calculated for a uniform visocisty mantle. The light, straight lines in Figures 7*a* and 7*b* show the two-dimensional half-space result, $K = -kd$. The dashed line at $K = 1$ gives the rigid earth result for comparison.

viscosity contrast above 670 km depth (model C) for $l = 7$ for the "FF" case. The lower viscosity in the upper mantle lessens the coupling between the flow and the upper surface, thereby decreasing the deformation of the upper surface and increasing that of the core-mantle boundary. In Figure 4*e* the coupling is so weak that self-gravitation actually causes the deformation to reverse, resulting in the slightly negative excursion of its mass displacement curve. This effect will be addressed more fully below.

Comparison of Figures 4*a* and 4*f* shows that the main effect of the no-slip condition, as opposed to the free-slip condition, at the upper surface is to restrict the flow near that boundary, resulting in more deformation and mass displacement at the upper boundary. This effect diminishes with increasing l as seen by comparison of Figures 4*b* and 4*g* as well as Figures 4*c* and 4*h*. Notice that for NF conditions the maximum mass displacement at the upper surface occurs with the load at depth rather than when it is nearest to the surface. A similar effect can be derived analytically for the two-dimensional case and is the result of flow restriction in a channel due to long-wavelength loading. In the three-dimensional (spherical) case this subsurface maximum in deformation is also enhanced considerably by the self-gravitation of the boundary. In addition to the stresses generated by the load "sinking" in the ambient (zeroth order) potential field there is a first-order perturbation in the ambient field due to both the load and the mass displacements at the boundaries. Although this idea is no more complicated than that of a self-consistent gravity field, the effect is physically subtle and warrants some discussion.

The basic propagator equations (18) are written for field variable six vectors, the last two terms of which are the perturbed geopotential field and its radial derivative (gravitational acceleration). These two variables must satisfy Poisson's equation independently, and it has recently been shown by R. J. O'Connell et al. (unpublished manuscript, 1984) that the 6×6 set of equations can be reduced to coupled 4×4 and 2×2 systems in which the 2×2 system involves only the potential variables and Poisson's equation. The 4×4 system is obtained by substitution of $u_3 + \rho^* u_5$ for u_3 in the six vector. This results in a decoupled four-vector system where

$$\mathbf{u}(6 \times 6) \rightarrow \mathbf{u}'(4 \times 4) = [v_r, v_\theta, r\tau_{rr}/\eta_0 + \rho r \delta V/\eta_0, r\tau_{r\theta}/\eta_0]^T$$

Physically, the normal stress term has been augmented by a "gravitational pressure" term, $\rho r \delta V/\eta_0$, to form a system of equations that is otherwise similar to the 4×4 propagator system used in two-dimensional problems [e.g., *Cathles*, 1975]. This formulation then shows explicitly how self-gravitation enters into the dynamics of the loading problem. Upon examination of the excitation vector (23) we notice that there are two driving terms: (1) The third term of the vector corresponds to the stress due to the density contrast being acted upon by the zeroth-order field, and (2) the sixth term represents the driving force due to the first-order field perturbation from the density contrast, that is, a gravitational pressure term. These extra pressure terms do not drive flow in steady state, but they do affect boundary deformations.

In Appendix 2 we discuss the problem of viscous relaxation to steady state in terms of the largest decay time associated with a given earth model. However, this approach constitutes a worst case analysis since all of the relaxation modes are, in general, excited by loading. Although we were able to justify the steady state assumption for our models even for these worst cases, it is possible with the analytical tools here to solve for mode excitation as a function of the depth of loading and harmonic degree. An eigenmode for the simple two-layer case can be represented by a unit normalized two vector giving the relative amount of mass displaced at the upper surface and the core-mantle boundary. For models A and C there is a mantle model (MO) and a core mode (C). For MO, both boundaries flex in the same sense; for the C mode their flexure is oppositely directed. The relative amounts of mode excitation are determined by finding the appropriate linear combination of MO and C required to give the boundary mass displacements in Figure 4. Note that this matching also solves the unloading problem, that is, excitation of modes due to the sudden release of an internal load of long duration; the loading and unloading problems are equivalent in terms of relative mode excitation. Figures 5*a*–5*c* show the results of the calculations for the FF models of Figure 4.

Figure 4 shows that at least for long-wavelength loads, the amount of mass displaced at the boundaries is comparable to the mass of the load itself, so the total geoid anomaly at the surface involves significant contributions from these sources.

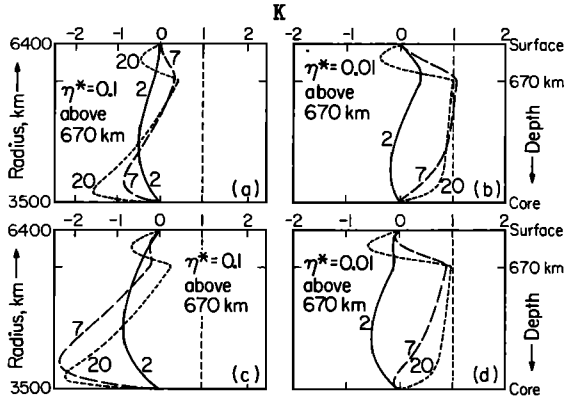

Fig. 8. Surface potential response K as a function of loading depth for viscosity contrasts of 0.1 and 0.01 in the upper mantle. Figures 8*a* and 8*b* are for FF boundary conditions and Figures 8*c* and 8*d* are for NF conditions.

Figure 6 shows the relative contribution from each of the three sources δV_a, δV_c, and δV_σ as functions of the depth of the load. The δV_σ ("σ") curve has a simple $(a/r)^{l+2}$ dependence derived solely from potential theory (see equation (A7)) and the δV_a ("a") and δV_c ("c") curves are proportional to the product of the mass displacement curves of Figure 4 and the $(a/r)^{l+2}$ factor. Potentials δV_a and δV_c are of opposite sign than δV_σ. Their absolute values are plotted normalized by the maximum value of δV_a to facilitate direct comparison. Figures 6*a*–6*c* are for FF conditions and Figures 6*d*–6*f* are for NF conditions. In most of the figures to follow we refer to potential anomalies since they are related to geoid anomalies simply through $\delta N = \delta V/g$, where δN is the geoid height due to δV and g is the gravitational acceleration at the surface. As was the case for the two-dimensional half space, the geoid contribution due to the deformation of the upper surface is generally larger than that due to the load. The contribution from the core-mantle boundary is generally small except for loads at great depth. Again, comparing Figures 6*a*–6*c* with Figures 6*d*–6*f*, the effect of stronger upper surface coupling due to the no-slip condition is evident. Notice that for $l = 2$ and $l = 7$ with NF conditions, the maximum δV_a contribution occurs at depth. In Figure 6*d* we have plotted (see curve "a'") the result obtained ignoring self-gravitation in order to demonstrate its importance for lower-degree harmonics. This was accomplished by ignoring the self-gravitation terms described above (at the expense of a self-consistent field). Since the difference between curve δV_σ and the sum of δV_a and δV_c determines the surface potential anomaly, this effect cannot be ignored for the lowest harmonic degrees.

The total surface potential δV_{tot} normalized by the load potential δV_σ results in the response function K, the modified Love number defined in (14). Figure 7 shows K as a function of loading depth and harmonic degree for the four possible combinations of boundary conditions. The differences among these results are not great although the relative coupling effects due to N or F conditions can be seen, especially for low-order harmonics. The cases with no slip at the core-mantle boundary are included because they simulate high viscosity in the lowermost mantle. In the more pertinent FF and NF cases, K is invariably negative for model A (no viscosity contrast). As predicted by (13), the magnitude of K can be much greater than unity; consequently, the geoid signature of a density contrast at depth is amplified. The straight light lines in Figures 7*a* and 7*b* show the two-dimensional half-space values for K. Note that with the load at either boundary,

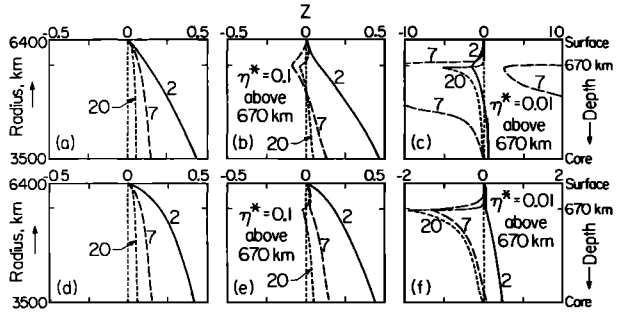

Fig. 9. Surface deformation impedance Z as a function of loading depth illustrating the effect of low viscosity in the upper mantle for harmonic degrees 2, 7, and 20. Figures 9*a*–9*c* are for FF boundary conditions and Figures 9*d*–9*f* are for NF conditions. The dashed line at $Z = 0$ gives the "perfect" compensation result for comparison.

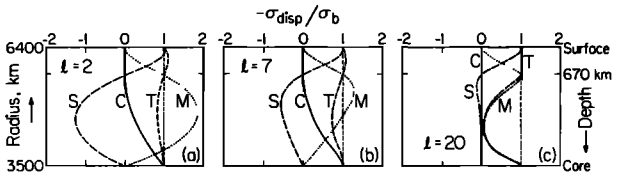

Fig. 10. Mass displacement at the boundaries as a function of loading depth for two-layer flow models with uniform viscosity (same as Figure 4 with additional displacement curve "M" for the 670-km discontinuity).

compensation of the geoid is complete to first order since all the loading stress is absorbed by deflection of the boundary. The geoid is much more sensitive to density contrasts in the middle regions of the mantle than to comparable density contrasts near boundaries.

The dominating influence of the upper surface deformation is diminished by the effect of low viscosity in the upper mantle resulting in less negative or even positive values of K. This is shown in Figure 8 for both FF and NF conditions. In this case the different boundary conditions result in more markedly different geoid signatures. The effect of the low-viscosity channel in the upper mantle is strongest for shorter wavelengths (larger l), whereas the channel is almost transparent to $l = 2$ loading. We have not presented many of the other models of viscosity stratification which are also plausible, but their effect can be roughly extrapolated from these figures. For example, a thinner channel, say 200 km thick, remains transparent to much shorter wavelengths than for the 670-km case.

The ratio of geoid anomaly to surface deformation, the impedance function Z (equation (17)), is shown in Figure 9 for models A and C for both FF and NF conditions. For uniform viscosity, Z is positive since the sign of the geoid is determined by the upper surface deformation. With a viscosity contrast the functions become more complicated and larger due to a reduced surface topographic signature. Note that singularities in Z can occur since the surface deformation can change sign (go through a zero) as seen for $l = 7$ in Figure 9*f*. In practical applications these singularities will be smoothed by integration over a depth distribution of density contrasts.

Layered Flow

The flow model representing a chemical discontinuity at 670 km depth is illustrated in Figure 1*b* corresponding to models D and E. Mass displacements at the boundaries are shown in Figure 10, comparable to Figure 4 for a uniform composition mantle. In these cases there is deformation and effective mass displacement at the layer boundary as shown by the "M" curves. For loads near the 670-km discontinuity the stress is taken up principally by the deformation of that boundary. The curves for total mass displacement in Figure 10, computed for NF boundary conditions, again represent dynamic compensation, as discussed for the case of whole mantle flow. The sense of flow in both the upper and lower mantle is reversed for loading in the upper mantle from that resulting from loading in the lower mantle. Consequently, the sign of both the core-mantle boundary and upper surface deformation depends upon whether the load is above or below the 670-km discontinuity; singularities occur in the corresponding impedance functions, and the behavior of K becomes more complicated. Figure 11 shows the relative excitation of viscous relaxation normal modes for these layered models where we now have an additional mode, M1, associated with deformation of the

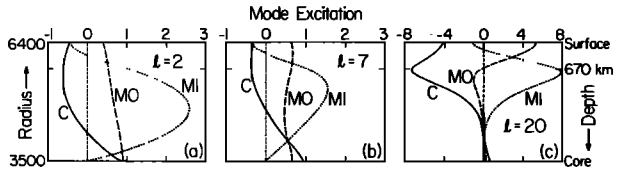

Fig. 11. Viscous normal mode excitation as a function of loading depth for two-layer flow models with uniform viscosity (same as Figure 5 with the additional M1 mode due to deformation of the 670-km discontinuity).

670-km discontinuity. The depth dependence for the MO and C mode is strikingly similar to that for the whole mantle case. The M1 mode is, as expected, dominant near the 670-km discontinuity.

The chemical layer response functions K and Z for models D and E are shown in Figures 12 and 13. The potential function K exhibits a more complicated depth dependence than for the whole mantle case. In particular, for no viscosity contrast the sign of the geoid anomaly reverses as we cross the 670-km discontinuity due to the dominance and reversal of the upper surface deformation; geoid anomalies due to correlated upper and lower mantle density contrasts are anticorrelated. Also, all functions K have an additional zero at 670 km depth. For a viscosity contrast at 670 km the coupling at the upper surface is reduced sufficiently so that the deformation of the 670-km discontinuity dominates the surface potential resulting again in negative values for K. Therefore a wide variety of behavior is possible for a relatively small range of viscosity contrasts (less than one order of magnitude).

Note that the maximum values of K for density contrasts in the upper mantle are small compared to those for the whole mantle flow model (Figure 7) and those for density contrasts in the lower mantle for the stratified models. The physical interpretation of this behavior is useful in developing intuition about dynamic geoid anomalies. As a first approximation, dynamic isostasy results in the conservation of mass in any column, at least at long wavelengths (see Figures 4 and 10). The total geoid anomaly results from a mass quadrupole consisting of a driving mass anomaly at depth and compensating mass anomalies at the deformed boundaries. The magnitude of the anomaly depends upon the separation of the boundaries: the "arm length" of the quadrupole. For a given mass anomaly the deeper the convecting layer, the larger the arm length and the greater the geoid anomaly. In the limit of zero thickness the geoid anomaly in a convecting layer goes to zero.

Upper surface impedance values, plotted in Figure 13, exhibit a singularity at 670 km and become very large for loads below this boundary with two orders of magnitude viscosity contrast. The sign and magnitude of Z for the chemical layer case is consequently a strongly varying function of depth, harmonic degree, and viscosity stratification; like K, it exhibits distinct (although not unique) characteristics that are highly model dependent.

INTERPRETATION

The range of solutions for K and Z obtained for the simple models we have described are illustrated in Figure 14. Instead of plotting K and Z as functions of depth and harmonic degree, we have now plotted them as functions of harmonic degree and earth model for representative depths of 300, 1400, and 2600 km in order to emphasize the most important conclusion resulting from this study: The relationship that exists among internal loading, surface deformation, and the geoid is a strong function not only of the depth and harmonic degree of loading but also the mechanical structure of the mantle. The dashed reference lines in Figures 14*a*–14*c* represent the value of K that would be observed for a rigid earth, that is, if we ignore the dynamic response. The impedance plots, Figures 14*d*–14*e*, have a $Z = 0$ reference line ("perfect" compensation) since Z becomes infinite for a rigid earth. Even the limited range of models we have explored exhibit a wide range of values for K and Z that indicate the sensitivity of the observables to structure. Interpretation of the earth's geoid in terms of internal processes demands careful consideration of a variety of physical effects, but much of the nonuniqueness inherent in surface gravity problems is removed because of the distinct signature of different models.

Figures 7–9 and 12–14 consititute "maps" that show how to relate geoid anomalies and surface deformations to the depth and harmonic degree of driving density contrasts. In most of the models there is roughly an order of magnitude amplification of the higher harmonic geoid anomalies for loads at great depth. For example, K attains its largest value of -12 in model A for $l = 20$ with the load several hundred kilometers above the core-mantle boundary. This requires modification of simple state-of-stress type arguments concerning the maximum geoid anomalies which can be generated by loads supported at great depth [*Kaula*, 1963*b*]. Required deviatoric stresses up to an order of magnitude smaller can support density contrasts generating a given geoid anomaly in dynamic earth models as opposed to an elastic model. Of course, these modified Love numbers must still be multiplied by $(r/a)^{l+2}$ to give the total potential (see *Hager*, this issue, Figure 4). Also from the figures showing K as a function of depth we see that to first order, K is zero at the boundaries, which implies that compensation of loads near boundaries is essentially complete. This means that bumps due to a variable thermal boundary layer in a convecting mantle are essentially masked out of the geoid signature. Since these density contrasts are likely to be among the largest associated with convection, this becomes a serious constraint on the resolvability of these features in the geoid. A good example of this is the observation that midoceanic ridges have very little long-wavelength geoid signature. Also in reference to the upper boundary layer, crustal and lithospheric thickness and density are not in general very well known for the earth. Application of the impedance response functions requires a more complete synthesis of information on lithospheric thickness and surface topography than is currently available, and this problem is currently under study. In addition to these complications it should be remembered that for a given density anomaly "map" for the mantle, say from seismic heterogeneity data or from a three-dimensional convection model, one must integrate $K(r, l)$ and $Z(r, l)$ over depth, as in (16) (the numerator δV and the de-

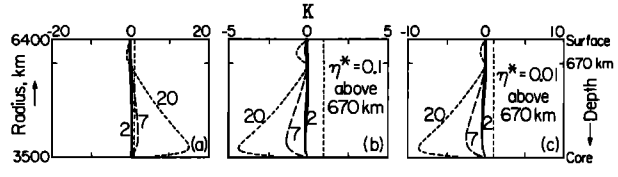

Fig. 12. Surface potential response K as a function of loading depth for two-layer models illustrating the effect of low viscosity in the upper mantle. Boundary conditions are no slip (N) at the surface and free slip (F) at the core-mantle boundary.

nominator $g\ \delta r$ of Z must be integrated separately). This will tend to smooth the respective models summarized in Figure 14. Another important point illustrated by these figures is that long-wavelength geoid anomalies are influenced more by density contrasts in the middle mantle than in the uppermost or lowermost mantle. Also, for a given range of density anomalies, whole mantle convection results in larger geoid anomalies than layered convection.

An example of the process of interpretation using dynamic response functions is found in *Hager*'s [this issue] analysis of the correlation between the geoid and subducted slabs as evidenced by deep focus earthquakes. Seismically active slabs represent known positive density contrasts that correlate spatially at better than the 99% confidence level in a positive sense with the degree 4–9 geoid. The positive correlation in this wavelength band requires an increase in viscosity with depth of two orders of magnitude between the upper and lower mantle in regions of active subduction. The amplitude of the observed geoid anomalies in the context of dynamic earth models requires much more excess mass than can be provided by subducted slabs alone in the upper mantle. A straightforward explanation is that the positive density contrasts associated with subduction extend into the lower mantle.

Seismology is now reaching the point where it is possible to map lateral velocity variations in the mantle. Examples include the determination of degree two lateral heterogeneity in the upper mantle by *Masters et al.* [1982], more detailed surface wave studies including odd and higher-order harmonics [*Nakanishi and Anderson*, 1982; *Woodhouse and Dziewonski*, this issue], and body wave studies of lateral velocity variations in the lower mantle [*Dziewonski et al.*, 1977; *Dziewonski*, this issue; *Clayton and Comer*, 1983]. When the velocity anomalies determined by these studies are compared to the observed geoid by assigning reasonable density contrasts to the velocity anomalies (neglecting the dynamical effects we have discussed), the geoids predicted are several times larger than those observed and are of opposite sign.

As we have shown in this paper, the dynamics of flow in the mantle can reduce the long-wavelength geoid anomalies from those resulting from the driving density contrasts alone and can even lead to a reversal in sign. Thus the seismological results are not qualitatively surprising. They are useful, when combined with the theory described here, in placing meaningful constraints on mantle dynamics. By combining observational seismology and the quantitative theory of dynamic geoid anomalies we can learn far more than we could by either technique alone. For example, B. H. Hager et al. (unpublished manuscript, 1984) have shown that 70% of the variance of the degree 2–3 geoid can be accounted for by seismically inferred density contrasts in the lower mantle, using the kernels of Figure 8*c*, for a model with uniform composition and an increase in viscosity of a factor of 10 across the 670-km discontinuity.

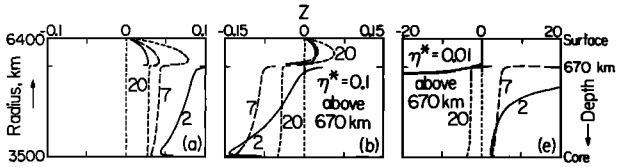

Fig. 13. Surface deformation impedance Z as a function of loading depth for two-layer models illustrating the effect of low viscosity in the upper mantle. (Dashed curves indicate singularities in Z.)

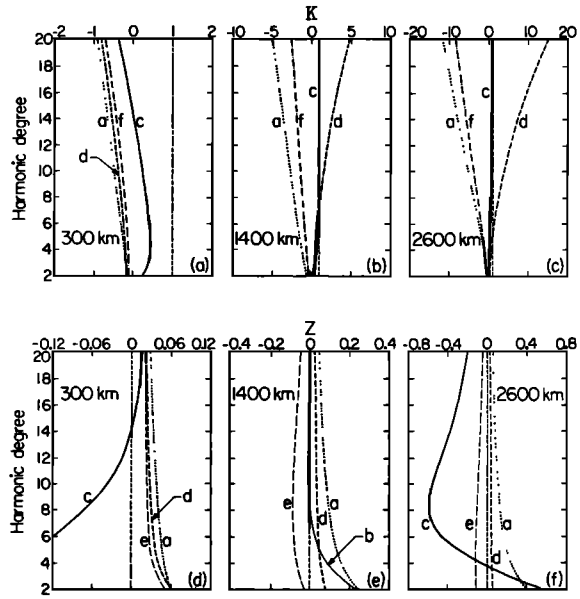

Fig. 14. Harmonic dependence of response functions K and Z for representative loading depths of 300, 1400, and 2600 km for a variety of models. Curves "a," "b," and "c" are for whole mantle flow with FF boundary conditions and upper mantle viscosity contrasts of 1.0, 0.1, and 0.01, respectively. Curves "d," "e," and "f" are for two-layer flow with NF boundary conditions and upper mantle viscosity contrasts of 1.0, 0.1, and 0.01.

The other geophysical observable we have discussed is surface deformation, which is expected to show a correlation with the long-wavelength geoid. Before this signature of mantle dynamics can be measured, however, the large effects of crustal thickness variations on topography must be removed. A simple, preliminary result is obtainable if we limit our comparison to old shield areas. For these areas, erosion can be assumed to have established a constant continental freeboard over geologic time. Also limiting our comparison to regions removed from collision zones, we find that the African shield, in a major geoid high, is high standing, while the Siberian and the Canadian shields, in major geoid lows, are relatively low standing [*NOAA*, 1980]. Similar conclusions can be reached from the hypsographic curves of *Harrison et al.* [1981]. From these observations we estimate that the impedance Z at long wavelengths is of order $+0.1$. This is consistent with the results for the long-wavelength correlation between seismic velocity heterogeneity in the lower mantle and the geoid. More detailed analysis using crustal thickness and density data should yield more accurate quantitative results over a broader spectral range.

Within the framework of a spherically symmetric model we are unable to reconcile the evidence from geoid anomalies over subduction zones that the effective viscosity increases by two orders of magnitude with the preliminary evidence from seismic studies and elevation of shield areas that the viscosity increases by only one order of magnitude. Perhaps not surprisingly, lateral variations in effective viscosity are suggested. Further theoretical improvements in our understanding of geoid anomalies in a dynamic earth are clearly desirable. Modeling of the effects of lateral viscosity variations and nonlinear rheology would be particularly useful in understanding the geoid signature of subducted slabs since they exist in zones characterized by large deviatoric stresses and temperature gradients. We would also like to model the effects of adiabatic

compressibility and adiabatic phase changes in the mantle. These improvements will require numerical modeling and would therefore imply a major departure from the analytical methods we have described.

SUMMARY

We have used spherical Newtonian earth models to investigate the relationship between driving loads and their geoid and surface topographic signatures. Normalized surface potential K and deformation impedance Z have been calculated for representative cases of viscous and chemical stratification in the mantle. The following dynamical effects are found to be important for geoid interpretation:

1. The response of the upper surface to loading has a large effect upon the behavior of the geoid signature, with negative geoid anomalies correlated with positive driving density contrasts for the simplest models without viscosity contrasts.
2. Considerable amplification of deep, higher harmonic loads is reflected in the geoid due to the manner in which flow stresses drive boundary deformation.
3. The choice of the upper surface boundary condition (free slip versus no slip) does not strongly effect the basic behavior of the response functions.
4. Lower viscosity in the upper mantle tends to drive K positive and Z toward larger values. For a very large viscosity contrast the upper surface deformation may reverse sign due to gravitational pressure resulting in a singularity in Z.
5. The introduction of a flow barrier corresponding to a chemical boundary has a pronounced effect on the magnitude of the response functions K and Z. In particular, density contrasts in the upper mantle have a much smaller geoid signature; this might help distinguish the two basic flow models when loads within the upper mantle can be estimated.
6. Near-boundary density contrasts are masked by the deformation of the boundary.
7. Self-gravitation is important for low harmonic degree loading.
8. Viscous relaxation of boundaries occurs on a much shorter time scale than convective flow so that boundary deformation due to internal loading can be considered steady state.
9. Applications of this theory to global data from geodesy and seismology show that the dynamical effects we have predicted can be observed for the earth. Improved analysis should yield a better understanding of mantle dynamics.

APPENDIX 1: ANALYTICAL DETAILS FOR THE WHOLE MANTLE PROBLEM

In order to solve equations (22) the boundary conditions (25) must be analytically continued to their respective spherical reference surfaces which are the mean earth radius a and the mean core radius c. The field variables are continued within the medium through which they are propagated in equations (22), in this case the mantle. To first order, the only terms in vectors (25) affected are the radial normal deviatoric stress and the gravitational acceleration. Since the stress above the earth's surface is zero, the normal deviatoric stress at the reference boundary is just the apparent jump described by equation (8), so

$$\mathbf{u}^N(a) = \left[0,\ 0,\ -\rho_m g(a) a\delta r/\eta_0,\ a\tau_{r\theta_a}/\eta_0,\ \rho_0 a\delta V_a/\eta_0,\ \frac{\rho_0 a^2}{\eta_0}\frac{\partial \delta V}{\partial t}\right]^T \tag{A1a}$$

or

$$\mathbf{u}^F(a) = \left[0,\ v_{\theta a},\ -\rho_m g(a)\delta r/\eta_0,\ 0,\ \rho_0 a\delta V_a/\eta_0,\ \frac{\rho_0 a^2}{\eta_0}\frac{\partial \delta V_a}{\partial r}\right]^T \tag{A1b}$$

At the core, using equation (6) and the perturbed hydrostatic stress, $-\rho_c \delta V_c$, at the reference level as seen in the mantle we obtain

$$\mathbf{u}^F(c) = \left[0,\ v_{\theta_c},\ \delta\rho_{cm} g(c) c\delta r_c/\eta_0 - \rho_c \delta V_c c/\eta_0,\ 0,\ \rho_0 c\delta V_c/\eta_0,\ \frac{\rho_0 c^2}{\eta_0}\frac{\partial \delta V_c}{\partial r}\right]^T \tag{A2}$$

Note that the normal stress term in this vector contains not only the effective stress discontinuity (proportional to δr_c) but also a gravitational pressure term (proportional to δV_c); this respresents the pressure field within the inviscid core.

The deformations δr_a and δr_c cause first-order perturbations in the potential δV in addition to that due to the driving density contrast σ at depth b. These perturbations are appropriately treated as effective surface masses at the reference boundary levels, as discussed above in our analytical treatment of boundary deformation. We now calculate the potential at $r = a$ (lithosphere) due to a surface mass distribution $\sigma = \Sigma_l \sigma_l$ at $r = b$. The perturbed potentials just above and below the surface are

$$\delta V_a^+ = \sum_l A_l \frac{a^l}{r^{l+1}} Y_l$$
$$\delta V_a^- = \sum_l A_l \frac{r^l}{a^{l+1}} Y_l \tag{A3}$$

since $\nabla^2 \delta V = 0$ away from the surface density contrast.

At the surface $\nabla^2 \delta V = 4\pi G\rho$ so, integrating over a volume Ω enclosed by a surface S,

$$\int_\Omega (4\pi G\rho)\, d\Omega = \int_\Omega \nabla^2(\delta V)\, d\Omega = \int_S \nabla(\delta V)\cdot \mathbf{n}\, da \tag{A4}$$

by Green's theorem. Integrating over a "pill box" containing a piece of the surface density contrast and shrinking the radial thickness of the box to zero, $\rho \to \sigma\, dr$, $\mathbf{n} \to \hat{r}$, $\nabla(\delta V) \to \partial(\delta V)/\partial r$ and (A4) becomes

$$\int_S \frac{\partial(\delta V)}{\partial r}\, da = \left[\frac{\partial(\delta V)}{\partial r}\right]_{a^-}^{a^+} = 4\pi G\sigma \tag{A5}$$

For our perturbed boundary conditions we impose an effective surface mass σ_{eff} such that the apparent jump in normal stress at the reference boundary is given by $\delta\tau_{rr_a} = g(a)\sigma_{\text{eff}}$. Expanding

$$\delta\tau_{rr_a} = \sum_l \delta\tau_{rr_a}{}^l Y_l$$

where we have made the lth harmonic dependence explicit, and using the above expansions for δV to calculate $[\partial(\delta V)/\partial r]_-{}^+$ we obtain the desired result:

$$\delta V_a^- = \frac{-4\pi G a}{g(a)} \sum_l \frac{\delta\tau_{rr_a}{}^l}{2l+1} (r/a)^l Y_l \tag{A6}$$

Similarly, at $r = c$ (core-mantle boundary) we obtain

$$\delta V_c^+ = \frac{4\pi G c}{g(c)} \sum_l \frac{\delta\tau_{rr_a}{}^l}{2l+1} (c/r)^{l+1} Y_l \tag{A7}$$

Again, for the density contrast at b,

$$\delta V_b^{+} = 4\pi G b \sum_l \frac{\sigma_l}{2l+1}(b/r)^{l+1} Y_l$$

$$\delta V_b^{-} = 4\pi G b \sum_l \frac{\sigma_l}{2l+1}(r/b)^{l} Y_l \tag{A8}$$

The total potentials at a and at c are given by

$$\delta V_a^{\text{tot}} = (\delta V_a^{-} + \delta V_c^{+} + \delta V_b^{+})_{r=a}$$
$$\delta V_c^{\text{tot}} = (\delta V_a^{-} + \delta V_c^{+} + \delta V_b^{-})_{r=c} \tag{A9}$$

These expressions contain explicitly the perturbed potentials due to boundary deformation that are required for a self-gravitating model. Writing the $\delta\tau_{rr}^{\ l}$ in terms of the δr, we obtain the following expressions for the potentials in terms of the stress variables and σ^l:

$$\delta V_a = \frac{4\pi G}{2l+1}\left[\frac{a}{g_a}\rho_m g(a)\delta r_a + \frac{c}{g_c}\left(\frac{c}{a}\right)^{l+1}\delta\rho_{cm} g(c)\delta r_c + b\left(\frac{b}{a}\right)^{l+1}\sigma^l\right]$$

$$\frac{\partial\delta V_a}{\partial r} = \frac{4\pi G}{2l+1}\left[\frac{l}{g_a}\rho_m g(a)\delta r_a - \frac{(l+1)}{g_c}\left(\frac{c}{a}\right)^{l+2}\delta\rho_{cm} g(c)\delta r_c - (l+1)\left(\frac{b}{a}\right)^{l+2}\sigma^l\right] \tag{A10}$$

$$\delta V_c = \frac{4\pi G}{2l+1}\left[\frac{a}{g_a}\left(\frac{c}{a}\right)^{l}\rho_m g(a)\delta r_a + \frac{c}{g_c}\delta\rho_{cm} g(c)\delta r_c + b\left(\frac{c}{b}\right)^{l}\sigma^l\right]$$

$$\frac{\partial\delta V_c}{\partial r} = \frac{4\pi G}{2l+1}\left[\frac{l}{g_a}\left(\frac{c}{a}\right)^{l-1}\rho_m g(a)\delta r_a - \frac{(l+1)}{g_c}\delta\rho_{cm} g(c)\delta r_c + l\left(\frac{c}{b}\right)^{l-1}\sigma^l\right]$$

Combining the first four of equations (21) with reference boundary expressions (A1a) and (A2) and potentials (A10), we obtain the following equations for δr_a and δr_c as well as $v_{\theta c}$ and $\tau_{r\theta_a}$:

$$\begin{aligned} P_{ca}^{\ i2} v_{\theta c} &+ \{P_{ca}^{\ i3}(1 - \rho_c{}^* cC/\eta_0) \\ &+ [P_{ca}^{\ i5} - (l+1)P_{ca}^{\ i6}]C\}\delta\rho_{cm} g(c)\delta r_c \\ &+ [(P_{ca}^{\ i5} + lP_{ca}^{\ i6})A - \delta_{i3} - P_{ca}^{\ i3}\rho_c{}^* aA/\eta_0] \\ &\cdot \rho_m g(a)\delta r_a - \delta_{i4} a\tau_{r\theta_a}/\eta_0 \\ &= -P_{ca}^{\ i3}\rho_c{}^* B - P_{ba}^{\ i3} bg(b)/\eta_0 + P_{ba}^{\ i6} 4\pi b^2 G\rho_0/\eta_0 \\ &- [P_c^{\ i5} + lP_c^{\ i6}]B \end{aligned} \tag{A11}$$

where

$$\mathbf{P}_{ca} = \mathbf{P}(a, c) \qquad \mathbf{P}_{ba} = \mathbf{P}(a, b) \qquad i = 1, 4$$

$$A = \frac{4\pi G\rho_0}{2l+1}\left(\frac{a}{g(a)}\right)\left(\frac{c}{a}\right)^{l+1}$$

$$B = \frac{4\pi G\rho_0}{2l+1}\left(\frac{c^2}{\eta_0}\right)\left(\frac{c}{b}\right)^{l-1}$$

$$C = \frac{4\pi G\rho_0}{2l+1}\left(\frac{c}{g(c)}\right)$$

and where the driving terms on the right are usually normalized by setting σ to unity. Exact values of the propagator elements $\mathbf{P}_{ca}^{\ ij}$, $\mathbf{P}_{ba}^{\ ij}$ can be calculated according to the procedures of *Hager and O'Connell* [1981] and (A11) can be solved in a straightforward manner. With these solutions for the boundary deformations and the potentials via (A10) we can calculate the kernels defined by (14)–(17).

Appendix 2: Viscous Relaxation Times for Spherical Earth Models

We need to demonstrate that the boundaries relax with time constants much smaller than the time scales for convective flow. These time constants can be obtained from consideraton of the normal mode problem for relaxation in a radially stratified viscous earth model. Viscoelastic solutions have been presented by *Wu and Peltier* [1982], but since convective time scales are far in excess of Maxwell times in the earth, the effect of elasticity can be ignored. The purely viscous normal mode problem is much less complicated and was first investigated by *Parsons* [1972]. Using propagator matrix methods which are described in detail by R. J. O'Connell et al. (unpublished manuscript, 1984), we have solved for the relaxation spectra of the self-gravitating spherical models used in the geoid calculations that follow. By setting all the stress-flow variables and boundary deformations proportional to exp $(-t/\tau_i)$ and solving the resulting system of homogeneous equations [see *Hager and O'Connell*, 1979] the eigenvalues τ_i as well as the eigenmodes for flow, stress, and deformation are obtained. Each flow boundary introduces an additional relaxation time constant and eigenmode. For example, for a simple model with an inviscid core overlain by a uniform mantle we obtain a mantle and a core mode. These modes are symmetric and antisymmetric respectively, with respect to the sense of boundary relaxation, and the time constant for the antisymmetric mode grows rapidly as the thickness of the flow layer decreases [*Solomon et al.*, 1982].

In Table 1 we have listed the parameters used for the models presented in this paper. Density values have been chosen to match the total mass of each layer (as well as the earth) and the gravity at each boundary [*Dziewonski et al.*, 1975], although with such a layering scheme it is impossible to match simultaneously other earth parameters, such as moment of inertia, which are not important to this study.

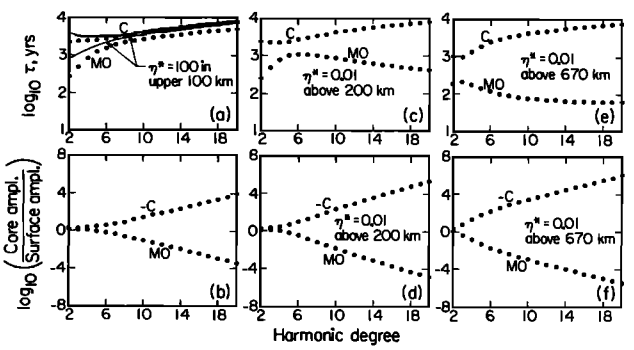

Fig. A1. Relaxation times and relative boundary discplacement amplitudes for viscous normal modes as functions of harmonic degree for whole mantle flow. M0 refers to the symmetric mantle mode and C refers to the asymmetric core mode. The notation "−C" in Figures A1b, A1d, and A1f emphasizes that the boundary deformations are of opposite sign for the core mode. The models represented include uniform mantle viscosity and low viscosity channels above 200 and 670 km depth. Figure A1a also shows the relatively minor effect of a high-viscosity "lithosphere" layer.

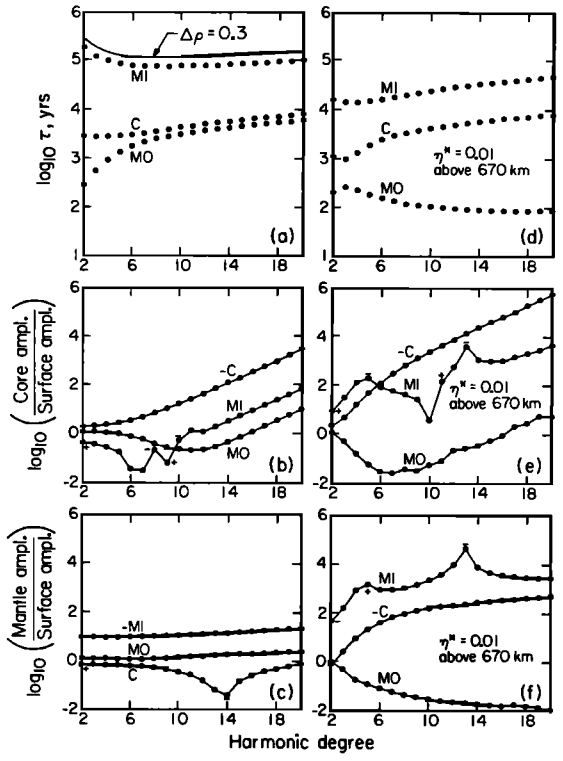

Fig. A2. Relaxation times and relative boundary amplitudes for viscous normal modes as functions of harmonic degree for two-layer flow. The M1 mode is generated by deformation of the flow barrier at 670 km depth, and the right-hand column of figures are for a low-viscosity upper mantle. Plus and minus signs on the amplitude curves indicate sign reversals in the sense of deformation relative to that of the surface. Figure A2*a* also shows the effect of using a density jump of 0.3 instead of 0.5 Mg/m^3 at the 670-km discontinuity.

Also, for the viscous relaxation problem we use smaller, more realistic density contrasts across internal boundaries (adiabatic compression in the mantle being ignored) since these values strongly affect the time constants obtained.

The two basic models used are those of whole mantle and layered mantle flow, both with an inviscid core. Arbitrary viscosity and density layering can be treated, so the models presented here are chosen to be illustrative rather than exhaustive. In Figures A1 and A2 we plot the relaxation time constants (eigenvalues) and the associated boundary deformations associated with each eigenmode. An individual eigenmode consists of a flow field throughout the mantle and could be represented as such. However, for our purposes the boundary deformations serve to identify both the appropriate branch (mode) and the relative excitation of each mode as we demonstrate later. Figures A1*a* and A1*b* show the results which are obtained for the uniform mantle model (model A). For each harmonic number l, following the nomenclature of *Peltier* [1976], there is a core mode (C) and a mantle mode (MO). For $l \leq 20$ the largest relaxation time obtained is less than 10^4 years and is associated with the C mode. Note that for high harmonic order the relaxation time increases with increasing wavenumber as in equation (10). In Figure A1*b* we plot the core deformation amplitude normalized by the surface deformation amplitude for each mode. As we would expect, the modes are strongly coupled at low harmonic order and relatively decoupled at higher values of l, thus distinguishing the C and MO mode branches. Also shown in Figure A1*a* is the very slight change in relaxation times caused by modeling the upper 100 km of mantle ("lithosphere") with two orders of magnitude higher viscosity than the mantle ($\eta = 10^{23}$ Pa s, or $\eta^* = \eta/\eta_0 = 100$ with $\eta_0 = 10^{21}$ Pa s denoting the reference or lower mantle viscosity). For the wavelengths of interest here such a layer is essentially transparent. In Figures A1*c* and A1*d* and A1*e* and A1*f* we illustrate the effect of low viscosity ($\eta^* = 0.01$) in the upper mantle above 200 and 670 km, respectively. There are three principal effects to be noted: (1) From the amplitude plots we see that the two modes tend to be decoupled by the low viscosity channel, (2) the C mode relaxation times are essentially unaffected while the mantle mode times are decreased by one to two orders of magnitude, and (3) the strength of these effects increases with the thickness of the low-viscosity channel. From these simple cases illustrating the effects of viscosity layering we conclude that for a broad class of whole mantle flow models, no relaxation times greater than 10^4 years are obtained for a lower mantle viscosity of 10^{21} Pa s.

We now consider models for two-layer, shear coupled flow in the mantle (models D and E) in which the depth of the top layer corresponds to the 670-km discontinuity. Since upper and lower mantle material do not mix across the 670-km discontinuity in these models we have introduced an internal boundary whose deformation contributes another mantle mode (M1). This boundary could be a chemical discontinuity or a phase boundary with sluggish kinetics. Figures A2*a*–A2*c* show the relaxation times, the relative deformation of the core-mantle boundary, and the relative deformation of the 670-km discontinuity for each of the modes C, M0, and M1, respectively. The relaxation times for the C and M0 modes are essentially the same as those obtained for the whole mantle case. However, the M1 mode has a much longer relaxation time (about 10^5 years). The boundary deformation amplitudes exhibit a much more complicated dependence upon l than for previous models, and the meaning of these eigenmodes will become more apparent when we address the problem of mode excitation; for now we will concentrate on the relaxation times. In particular, when the density contrast across the 670-km discontinuity is decreased from 0.5 to 0.3 Mg/m^3 a significant increase in the M1 time occurs (Figure A2*a*). This can be easily understood physically since the buoyancy force that tends to restore a boundary to its reference configuration is proportional to the density jump, $\delta\rho$, at that boundary. Therefore as $\delta\rho$ is made smaller, the associated relaxation time increases accordingly. Since the actual density contrasts within the earth are not exactly known, it is important to remember this effect when modeling relaxation times. In Figures A2*d*–A2*f* we illustrate the effects of low viscosity in the upper mantle for two-layer flow. Both the M0 and M1 modes accordingly exhibit smaller relaxation times, the effect on M1 being one half to one order of magnitude. We conclude that for the two-layer flow model the longest relaxation time expected is about 10^5 years. An upper mantle flow layer involving chemical boundaries at say 400 or 220 km [*Anderson*, 1979] would result in longer relaxation times, but we have not included these more complicated cases in our geoid models.

None of the relaxation times calculated so far have been in excess of 10^5 years, which for reasonable mantle flow velocities would allow for about 10 km transport in the mantle. This is indeed small compared to the flow dimensions, so for lower mantle viscosities of 10^{21} Pa s, the assumption of steady state flow is verified. Recent studies by *Peltier* [1981] and *Yuen et al.* [1982] indicate that the viscosity of the lower mantle is less than 10^{22} Pa s. Since the relaxation problem scales linearly

with reference viscosity (which we always take to be that of the lower mantle), it is not likely that the steady state hypothesis for boundary deformation is seriously violated for the overall convective circulation in the mantle. Alternatively, computing the ratio of flow velocity to the velocity of relaxation of the boundary as in equation (12), the viscosity cancels, indicating that boundaries relax rapidly relative to changes in the flow regime whatever the mantle viscosity.

Acknowledgments. We thank Don L. Anderson for stimulating discussion and R. J. O'Connell, Roger Phillips, and an anonymous reviewer for very useful comments on the manuscript. This work was supported by NASA grants NSG-7610, NAG-5315 and NAS5-27226 and an Alfred P. Sloan Foundation Fellowship awarded to B. H. Hager. Contribution 3981, Division of Geological and Planetary Sciences, California Institute of Technology, Pasadena, California 91125.

REFERENCES

Anderson, D. L., Chemical stratification of the mantle, *J. Geophys. Res.*, *84*, 6297–6298, 1979.

Ashby, M. F., and R. A. Verrall, Micromechanisms of flow and fracture, and their relevance to the rheology of the upper mantle, *Philos. Trans. R. Soc. London Ser. A*, *288*, 59–95, 1977.

Berckhemer, H., F. Auer, and J. Drisler, High temperature anelasticity and elasticity of mantle peridotites, *Phys. Earth Planet. Inter.*, *20*, 48–59, 1979.

Cathles, L. M., III, *The Viscosity of the Earth's Mantle*, Princeton University Press, Princeton, N. J., 1975.

Chase, C. G., Subduction, the geoid, and lower mantle convection, *Nature*, *282*, 464–468, 1979.

Chase, C. G., and M. K. McNutt, The geoid: Effect of compensated topography and uncompensated oceanic trenches, *Geophys. Res. Lett.*, *9*, 29–32, 1982.

Clark, J. A., W. F. Farrell, and W. P. Peltier, Global changes in postglacial sea level: A numerical calculation, *Quat. Res.*, *9*, 265–287, 1978.

Clayton, R. W., and R. P. Comer, A tomographic analysis of mantle heterogeneities from body wave travel times (abstract) *Eos Trans. AGU*, *62*, 776, 1983.

Crough, S. T., and D. M. Jurdy, Subducted lithosphere, hotspots, and the geoid, *Earth. Planet. Sci. Lett.*, *48*, 15–22, 1980.

Dziewonski, A. M., Mapping the lower mantle: Determination of lateral heterogeneity in *P* velocity up to degree and order 6, *J. Geophys. Res.*, this issue.

Dziewonski, A. M., and R. A. W. Haddon, The radius of the core-mantle boundary inferred from travel time and free oscillation data: A critical review, *Phys. Earth. Planet. Inter.*, *9*, 28–35, 1974.

Dziewonski, A. M., A. L. Hales, and E. R. Lapwood, Parametrically simple earth models consistent with geophysical data, *Phys. Earth Planet. Inter.*, *10*, 12, 1975.

Dziewonski, A. M., B. H. Hager, and R. J. O'Connell, Large-scale heterogeneities in the lower mantle, *J. Geophys. Res.*, *82*, 239–255, 1977.

Gantmacher, F. R., *The Theory of Matrices*, vols. 1 and 2, translated from Russian by K. A. Hirsch, Chelsea, New York, 1960.

Guier, W. H., Determination of the non-zonal harmonics of the geopotential from satellite Doppler data, *Nature*, *200*, 124–125, 1963.

Hager, B. H., Global isostatic geoid anomalies for plate and boundary layer models of the lithosphere, *Earth Planet. Sci. Let.*, *63*, 97–109, 1983.

Hager, B. H., Subducted slabs and the geoid; constraints on mantle rheology and flow, *J. Geophys. Res.*, this issue.

Hager, B. H., and R. J. O'Connell, Subduction zone dip angles and flow driven by plate motion, *Tectonophysics*, *50*, 111–133, 1978.

Hager, B. H., and R. J. O'Connell, Kinemetic models of large-scale mantle flow, *J. Geophys. Res.*, *84*, 1031–1048, 1979.

Hager, B. H., and R. J. O'Connell, A simple global model of plate dynamics and mantle convection, *J. Geophys. Res.*, *86*, 4843–4867, 1981.

Harrison, C. G. A., G. W. Brass, E. Saltzman, J. Sloan II, J. Southam, and J. M. Whitman, Sea level variations, global sedimentation rates, and the hypsographic curve, *Earth Planet. Sci. Lett.*, *54*, 1–16, 1981.

Haskell, N. A., The motion of a viscous fluid under a surface load, *Physics*, *6*, 265–269, 1935.

Jacobsen, S. B., and G. J. Wasserburg, A two-reservoir recycling model for mantle-crust evolution, *Proc. Natl. Acad. Sci. U.S.A.*, *77*, 6298–6302, 1980.

Jarvis, G. T., and D. P. McKenzie, Convection in a compressible fluid with infinite Prandtl number, *J. Fluid Mech.*, *96*, 515–583, 1980.

Kaula, W. M., Tesseral harmonics of the gravitational field and geodetic datum shifts derived from camera observations of satellites, *J. Geophys. Res.*, *68*, 473–484, 1963*a*.

Kaula, W. M., Elastic models of the mantle corresponding to variations in the external gravity field, *J. Geophys. Res.*, *68*, 4967–4978, 1963*b*.

Kaula, W. M., Global gravity and tectonics, in *The Nature of the Solid Earth*, edited by E. C. Robertson, pp. 386–405, McGraw-Hill, New York, 1972.

Love, A. E. H., *Some Problems of Geodynamics*, Dover, New York, 1911.

Masters, G., T. H. Jordan, P. G. Silver, and F. Gilbert, Aspherical earth structure from fundamental spheroidal-mode data, *Nature*, *298*, 609–613, 1982.

McKenzie, D. P., Surface deformation, gravity anomalies and convection, *Geophys. J. R. Astron. Soc.*, *48*, 211–238, 1977.

McKenzie, D. P., and C. Bowin, The relationship between bathymetry and gravity in the Atlantic ocean, *J. Geophys. Res.*, *81*, 1903–1915, 1976.

Morgan, W. J., Gravity anomalies and convection currents, 1, A sphere and cylinder sinking beneath the surface of a viscous fluid, *J. Geophys. Res.*, *70*, 6175–6185, 1965.

Munk, W. H., and G. J. F. MacDonald, *The Rotation of the Earth: A Geophysical Discussion*, Cambridge University Press, New York, 1960.

Nakanishi, I., and D. L. Anderson, Worldwide distribution of group velocity of mantle Rayleigh waves as determined by spherical harmonic inversion, *Bull. Seismol. Soc. Am.*, *72*, 1183–1192, 1982.

National Oceanic and Atmospheric Administration, Topographic data for one-degree size areas, Environ. Data Serv., NGS Data Cent., Boulder, Colo., 1980.

O'Connell, R. J., Pleistocene glaciation and the viscosity of the lower mantle, *Geophys. J. R. Astron. Soc.*, *23*, 299–327, 1971.

Parsons, B. E., Changes in the earth's shape, Ph.D. thesis, Cambridge Univ., Cambridge, United Kingdom, 1972.

Parsons, B., and S. Daly, The relationship between surface topography, gravity anomalies and the temperature structure of convection, *J. Geophys. Res.*, *88*, 1129–1144, 1983.

Passey, Q. R., Upper mantle viscosity derived from the difference in rebound of the Provo and Bonneville shorelines: Lake Bonneville Basin, Utah, *J. Geophys. Res.*, *86*, 11701–11708, 1981.

Pekeris, C. L., Thermal convection in the interior of the earth, *Mon. Not. R. Astron. Soc., Geophys. Suppl.*, *3*, 343–367, 1935.

Peltier, W. R., Glacio-isostatic adjustment, II, The inverse problem, *Geophys. J. R. Astron. Soc.*, *46*, 669–705, 1976.

Peltier, W. R., Ice age geodynamics, *Annu. Rev. Earth Planet. Sci.*, *9*, 199–225, 1981.

Ricard, Y., L. Fleitout, and C. Froidevaux, Geoid heights and lithospheric stresses for a dynamical earth, *Ann. Geophys.*, in press, 1983.

Richards, M. A., and B. H. Hager, A dynamically consistent calculation of geoid anaomalies in a viscous planet with implications for geoid interpretation (abstract), *Eos Trans. AGU*, *62*, 1077, 1981.

Richter, F. M., and D. P. McKenzie, On some consequences and possible causes of layered convection, *J. Geophys. Res.*, *86*, 6133–6142, 1981.

Runcorn, S. K., Satellite gravity measurements and a laminar viscous flow model of the earth's mantle, *J. Geophys. Res.*, *69*, 4389–4394, 1964.

Runcorn, S. K., Flow in the mantle inferred from the low degree harmonics of the geopotential, *Geophys. J. R. Astron. Soc.*, *14*, 375–384, 1967.

Solomon, S. C., R. P. Comer, and J. W. Head, The evolution of impact basins: Viscous relaxation of topographic relief, *J. Geophys. Res.*, *87*, 3975–3992, 1982.

Twiss, R. J., Structural superplastic creep and linear viscosity in the earth's mantle, *Earth Planet. Sci. Lett.*, *33*, 86–100, 1976.

Watts, A. B., An analysis of isostasy in the world's oceans, 1, Hawaiian-Emperor seamount chain, *J. Geophys. Res.*, *83*, 5989–6004, 1978.

Weertman, J., Dislocation climb theory of steady-state creep, *Trans. Am. Soc. Met*, *61*, 681–694, 1968.

Woodhouse, J. H., and A. M. Dziewonski, Mapping the upper mantle: Three-dimensional modeling of earth structure by inversion of seismic waveforms, *J. Geophys. Res.*, this issue.

Wu, P., and W. R. Peltier, Viscous gravitational relaxation, *Geophys. J. R. Astron. Soc.*, *70*, 435–486, 1982.

Yuen, D. A., R. Sabadini, and E. V. Boschi, Viscosity of the lower mantle as inferred from rotational data, *J. Geophys. Res.*, *87*, 10745–10762, 1982.

B. H. Hager and M. A. Richards, Seismological Laboratory, 252-21, California Institute of Technology, Pasadena, CA 91125.

(Received September 28, 1983;
revised April 18, 1984;
accepted April 18, 1984.)